Optimal elastic source wavefield reconstruction

Ivan Lim Chen Ning & Paul Sava
Center for Wave Phenomena, Colorado School of Mines

ABSTRACT

Reverse time migration (RTM) is capable of producing seismic images of complex geology by correlating extrapolated source and receiver wavefields. RTM is commonly regarded as a memory intensive operation because the source and receiver are not synchronous, which fundamentally require wavefield storage. Many methods are proposed to manipulate the source wavefield efficiently, such as storing the wavefield in the boundary layer followed by its reconstruction as necessary. However, the memory requirement is still considerably voluminous due to the need to save at least several layers around the computational zone. By using the integral solution of the representation theorem enclosing the computational volume, we can reduce the boundary storage to a single layer and still precisely extrapolate the wavefield back into the volume. Building on this idea, we propose the reconstruction of the source wavefield for elastic RTM and waveform inversion from a single layer of the boundary enclosing the computational domain. This reduces the memory and the computational requirements, which is especially important for large-scale 3D experiments. Numerical example demonstrates the effectiveness of our proposed method to successfully reconstruct the source wavefield from a single boundary layer without lessening the ability produce accurate representations of the subsurface of arbitrary anisotropy and heterogeneity.

Key words: reverse time migration, finite difference, representation theorem

1 INTRODUCTION

Reverse time migration (RTM) is a household name in the world of exploration seismology and has become one of the primary workhorses for subsurface seismic imaging in complex geologic settings. The underlying principle of RTM involves correlation of source and receiver wavefields reconstructed in the entire image space. These wavefields are obtained through forward and backward wavefield extrapolation from the source function and the recorded data, respectively. For correlation, the two wavefields need to be available at all times and positions. A naive implementation of RTM would compute and save both source and receiver wavefields prior to correlation. For large-scale 3D experiments, accessing such large 4D (space and time) hypercubes is hugely expensive, both regarding storage and I/O. Since the RTM imaging condition implies zero-lag crosscorrelation, we can lessen the storage burden by accruing the image gradually as we access the reconstructed wavefields. Doing so requires wavefields readily available for simultaneous access which suggests large storage and costly I/O. Per contra, there are ways to efficiently store parts of the source wavefield to be reconstructed on the fly as we extrapolate the receiver wavefields backward in time. This approach reduces the I/O load significantly by a slight increase in computation cost.

A natural way to address the storage problem is to save intermediate time snapshots of the source wavefield hypercube and recursively fill in the wavefield at other times when necessary for correlation with the receiver wavefield (Symes, 2007; Anderson et al., 2012). This method is known as optimal checkpointing which is effective, yet still memory and computationally intensive. An alternative to significantly reduce storage requirements while reconstructing the source wavefield is to store the wavefield at a conventional boundary (Dussaud et al., 2008; Nguyen and McMechan, 2014; Yang et al., 2014) or a random boundary (Clapp, 2009; Shen and Clapp, 2011, 2015; Jia and Yang, 2017). Since the deployment of the random boundary reconstructs the source wavefield at the price of slight artifacts from the generation of scattered wavefields due to the random perturbations of material properties in the boundary zone, we focus on methods that utilize the conventional boundary method. Accurate reconstruction of the source wavefield from the boundary requires storage of at least half the finite-difference stencil size. We can achieve further storage reduction by saving intermediate time steps, followed by filling in through interpolation (Yang et al., 2016). However,

as we increase the accuracy of finite-difference, the boundary layer required for reconstruction increases along with the storage volume. Reducing the boundary layer size can be accomplished by linear combination of the wavefields along the boundary at the expense of modest reconstruction errors (Liu et al., 2015). An alternative is to gradual reduce the finite-difference order as we approach the boundary, yet again with loss of accuracy (Bo and Huazhong, 2011). To further decrease storage at a single boundary layer and maintain accuracy, one can improve the reconstruction through the Lax-Wendroff method by obtaining spatial derivative from temporal derivatives on the boundary (Tan and Huang, 2014; Mulder, 2017).

As an alternative to achieve significant memory storage reduction, we can use the representation theorem as the main mechanism to reconstruct wavefields from minimal information available on the boundary of the domain through deployment of so-called the multiple point sources. The source wavefield recorded on a single boundary layer (the surface) is reconstructed via multiple point source injection into the computational domain which is equivalent to the integral solution of the representation theorem (Aki and Richards, 2002; Wapenaar, 2014). This method is successfully demonstrated by Vasmel and Robertsson (2016), using the acoustic wave approximation.

The acoustic approximation is inadequate to accurately characterize the Earth's elastic subsurface. However, imaging methods based on the full elastic anisotropic wave equation are both expensive computationally and from the storage perspective. Ravasi and Curtis (2013) exploit the representation theorem for exact elastic wavefield extrapolation that avoids nonphysical waves, i.e., wave modes reconstructed during reverse-time extrapolation that were not present in the observed data. In this paper, we utilize the representation theorem to accurately reconstruct the elastic source wavefield from data stored on a single boundary layer. This methodology is applicable to memory intensive applications such as elastic RTM or elastic waveform tomography. Raknes and Weibull (2016) demonstrate an reconstruction through approximating the representation theorem at the cost of generating nonphysical wave modes. In this paper, we honor the full representation theorem as we illustrate the feasibility of this method numerical examples of elastic RTM using forward-propagated wavefields and reconstructed wavefields derived from stored boundaries.

2 THEORY

We describe elastic-wave propagation using the second-order partial differential equations formulated with the stress $\underline{\mathbf{t}}$ tensor and the particle displacement $\mathbf{u}$ vector (Aki and Richards, 2002)

$$\rho\,\frac{\partial^2\mathbf{u}}{\partial t^2} = \nabla\cdot\underline{\mathbf{t}} + \mathbf{f}\,, \tag{1}$$

where $\rho\,(\mathbf{x})$ is the density and $\mathbf{f}\,(\mathbf{x},t)$ is the external volume force. The stress $\underline{\mathbf{t}}\,(\mathbf{x},t)$ and strain $\underline{\mathbf{e}}\,(\mathbf{x},t)$ tensors are related through the constitutive relation with the assumption of linear elasticity by

$$\underline{\mathbf{t}} = \underline{\underline{\mathbf{c}}}\,\underline{\mathbf{e}} + \underline{\mathbf{m}}\,, \tag{2}$$

where $\underline{\mathbf{h}}\,(\mathbf{x},t)$ is the external deformation source which together with stiffness tensor $\underline{\underline{\mathbf{c}}}\,(\mathbf{x})$ to forms a stress perturbation source $\underline{\underline{\mathbf{c}}}\,(\mathbf{x})\;\underline{\mathbf{h}}\,(\mathbf{x},t)$. The relationship between the strain tensor and the particle displacement is

$$\underline{\mathbf{e}} = \frac{1}{2}\left\{\nabla\mathbf{u} + (\nabla\mathbf{u})^{\intercal}\right\}\,, \tag{3}$$

The representation theorem for the corresponding equations is (Aki and Richards, 2002):

$$\mathbf{u}(\mathbf{x}) = \iiint_{\Omega} dV\;\mathbf{f}(\boldsymbol{\xi}) * \mathbf{G}(\mathbf{x},\boldsymbol{\xi}) + \oiint_{\partial\Omega} ds\;\left\{\underline{\mathbf{t}}(\boldsymbol{\xi}) * \mathbf{G}(\mathbf{x},\boldsymbol{\xi}) - \underline{\underline{\mathbf{c}}}\,\mathbf{u}(\boldsymbol{\xi}) * \frac{\partial\mathbf{G}(\mathbf{x},\boldsymbol{\xi})}{\partial\boldsymbol{\xi}}\right\}\cdot\mathbf{n}\,, \tag{4}$$

where $*$ denotes time convolution. $\boldsymbol{\xi}$ and $\mathbf{x}$ are the source and evaluation locations respectively. The vector $\mathbf{n}$ is the normal to the closed surface $\partial\Omega$. Figure 1 describes the physical elements of the representation theorem. If we assume that there are no external volume forces $\mathbf{f}$ present, the volume integral vanishes. The surface integral vanishes if we assume a homogeneous boundary condition (Gangi, 1970). When the traction $\underline{\mathbf{t}}\cdot\mathbf{n}$ and the displacement $\mathbf{u}$ on the surface $\partial\Omega$ enclosing the volume Ω are excited from the external volume force $\mathbf{f}$ within the volume, i.e. data recorded on a surface, we can express the particle displacement $\mathbf{v}$ wavefield inside the volume Ω surrounded by the surface $\partial\Omega$ as

$$\mathbf{v}(\mathbf{x}) = -\oiint_{\partial\Omega} ds\;\left\{\underline{\mathbf{t}}(\boldsymbol{\xi}) * \mathbf{G}(\mathbf{x},\boldsymbol{\xi}) - \underline{\underline{\mathbf{c}}}\,\mathbf{u}(\boldsymbol{\xi}) * \frac{\partial\mathbf{G}(\mathbf{x},\boldsymbol{\xi})}{\partial\boldsymbol{\xi}}\right\}\cdot\mathbf{n}\,. \tag{5}$$

The Green's function $\mathbf{G}(\mathbf{x},\boldsymbol{\xi})$ in equation 5 denotes a wave-propagator using the external volume force $\mathbf{f}$ as source. The stiffness tensor $\underline{\underline{\mathbf{c}}}$ together with the spatial derivative of the Green's function $\partial\bar{\bar{\mathbf{G}}}(\mathbf{x},\boldsymbol{\xi})/\partial\boldsymbol{\xi}$ in equation 5 form the equivalent of a wave-propagator using an external deformation force $\underline{\mathbf{h}}$ as the source in reverse-time propagation, the sign in the

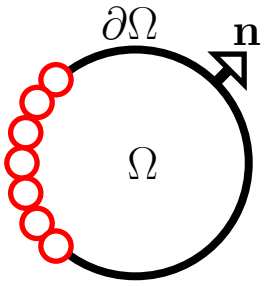


Figure 1. Schematic diagram to illustrate the elements of the representation theorem. The black circle denotes the surface $\partial\Omega$ enclosing a volume Ω with the corresponding normal vector $\mathbf{n}$ pointing outwards. The red circles denotes the locations of sources/receivers.

integral changes to negative to denote backward propagating Green's function (Wapenaar, 2014).

To obtain the integral solution of the representation theorem, we use the multiple point sources method to turn the saved wavefield along the boundary $\partial\Omega$ into sources. In order to reconstruct the source wavefield using the representation theorem, we save the source wavefield along the boundary $\partial\Omega$ (black dots) as highlighted in Figure 2(a) which requires less memory than conventional methods. The conventional boundary methods reconstruct the source wavefield by storing at least half (Yang et al., 2014) of the finite-difference stencil size as shown in Figure 2(b).

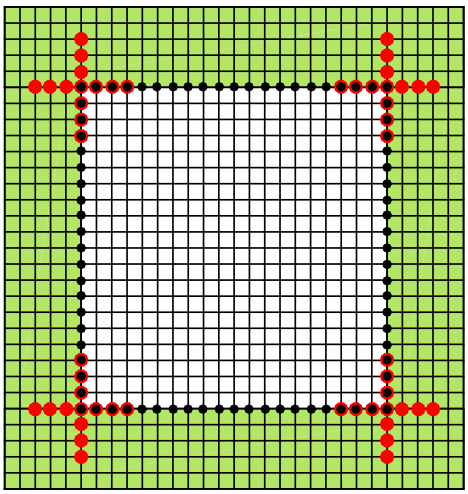
Our primary goal in this paper is to perform elastic RTM by reconstructing the source wavefield on the fly. To avoid comparing multiple elastic RTM images for a given experiment, we adopt the energy imaging condition (Rocha et al., 2017) which generates a single elastic image without wavemode decomposition. We modify the potential term of the imaging condition to exploit the forward simulated displacement and stress wavefields $(\mathbf{u}, \underline{\underline{\mathbf{t}}})$ together with the adjoint displacement and strain wavefields $\left(\mathbf{u}^{\dagger}, \underline{\underline{\mathbf{e}}}^{\dagger}\right)$

$$\begin{aligned}\mathbf{I} &= \sum_{e,t}\left[\rho\dot{\mathbf{u}}\cdot\dot{\mathbf{u}}^{\dagger} - \left(\underline{\underline{\mathbf{c}}}\,\underline{\underline{\mathbf{e}}}\right)\cdot\underline{\underline{\mathbf{e}}}^{\dagger}\right] \\ &= \sum_{e,t}\left[\rho\dot{\mathbf{u}}\cdot\dot{\mathbf{u}}^{\dagger} - \quad \underline{\underline{\mathbf{t}}}\ \cdot\underline{\underline{\mathbf{e}}}^{\dagger}\right]\end{aligned} \tag{6}$$

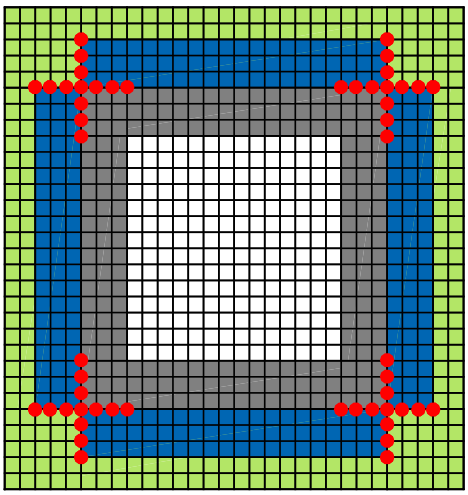
where the image $\mathbf{I}(\mathbf{x})$ is formed by summation over experiment e. The dot $(\dot{})$ represents time derivative, and the dagger $(^{\dagger})$ denotes adjoint. The reformulation allows us to avoid the additional re-computation of wavefield derivatives in the kinetic term of the imaging condition as we solve equation 1 through the elastodynamic relationship. As pointed out by Rocha et al. (2017), the source and receiver particle velocity $\left(\dot{\mathbf{u}}, \dot{\mathbf{u}}^{\dagger}\right)$ wavefields describe the kinetic energy term, and the elastic strain $\left(\underline{\underline{\mathbf{c}}}\,\underline{\underline{\mathbf{e}}}, \underline{\underline{\mathbf{e}}}^{\dagger}\right)$ gives the potential energy term. The imaging condition represents the Lagrangian density, the difference between kinetic and potential energy.

3 SOURCE RECONSTRUCTION EXAMPLE

In reconstructing the source wavefield, we first perform a forward propagation in time and save the wavefield at a single layer between the computational and boundary domains, as shown in Figure 2(a). Wavefield computation occurs in the volume Ω, and the single layer where we store the source wavefield in the boundary $\partial\Omega$, equation 5. The source wavefield is reconstructed backward in time together with the receiver wavefield. To illustrate the theory numerically, we use a simple two-layer elastic model with the P-wave velocity shown in Figure 3(a). The S-wave and density are constant. When comparing the source wavefield, we save the forward extrapolated source wavefield to serve as a reference for the wavefield reconstructed from the boundary $\partial\Omega$ using the representation theorem. We present the wavefield displays in the following tensor-vector matrix layout



(a)



(b)

Figure 2. An example for computational (in white) and boundary domain (in green) set up. (a) Our method to reconstruct the source wavefield only require storage at a single boundary layer (black dots). (b) Conventional methods require storage at half the finite-difference stencil either in the computational (in gray) or in the boundary (in blue) domain. Our method in (a) shows significant reduction for storage requirement compared to conventional methods in (b).

$$\begin{array}{|c|c|c|}\hline \mathrm{t}_{xx} & \mathrm{t}_{xy} & \mathrm{t}_{xz} \\ \hline \mathrm{u}_{x} & \mathrm{t}_{yy} & \mathrm{t}_{yz} \\ \hline \mathrm{u}_{y} & \mathrm{u}_{z} & \mathrm{t}_{zz} \\ \hline\end{array}\ ,$$

where we combine the stress tensor in its natural matrix form

together with the particle displacement vector wavefield. In the case of 2D simulations confined to the xz-plane, the corresponding y-components are left empty. Figure 4 shows the reference source wavefield at 3 different time snapshots using an explosive type source from the location of the white dot shown in Figure 3(a) at $(0.075 \text{ km}, 0.005 \text{ km})$. Figure 5 shows the corresponding reconstructed source wavefield. We evaluate the accuracy of the reconstruction by analyzing the difference wavefield plots between reference and reconstruction in Figure 6. The subtle amplitudes in the difference plot are due to the weak reflections from imperfect absorbing boundary condition. The four corners of the computational domain contribute towards the amplitudes in the difference plot as well. At the corner points, the normal vectors $\mathbf{n}$ are undefined which may cause the generation of artifacts during reconstruction. A possible solution is to adopt the superellipse geometry in place of the rectangle.

To further examine the reconstruction accuracy, we graph the wavefields along the x-axis at a depth of 0.025 km. Figure 7 shows the graphs for the reference source wavefield (in blue) overlaid on the reconstructed source wavefield (in red) for the same time snapshots as in Figure 4 and 5. The small ripple like artifacts in Figure 6 are due to the corner points.

4 RTM EXAMPLE

Notwithstanding a successful reconstruction of the source wavefield, we apply the method to elastic RTM using the energy norm imaging condition, equation 6. Figure 3(b) shows the smooth velocity model for RTM. Again, we use the reference wavefield to produce the reference energy norm RTM image. This reference image is based on the so-called full wavefield storage method (Nguyen and McMechan, 2014). Figure 8 depict images for a single shot of the reference image, Figure 8(a) and for the reconstructed source wavefield, Figure 8(b) as well as the difference, Figure 8(c). At a glance, the grayscale images do not show much difference between Figure 8(a) and 8(a). The only noticeable amplitudes from the difference plot in Figure 8(c) are due to the imperfect absorbing boundary condition and corner points artifacts in the source wavefield reconstruction. Note that there is a small amplitude difference between the source location in Figure 8(b). The amplitude are correlations between the receiver and source wavefield reconstruction in reverse time where the source wavefield continues to expand after collapsing at the source location at the wavelet peak time.

We also extract amplitude profiles along the z-axis (vertical dotted line) at the shot location and along the x-axis (horizontal dotted line) at the reflection depth in Figure 8. Figures 8(a) and 8(b) show the same amplitude profile with the reference image (in blue) overlaid with the reconstructed source wavefield image (in red). The amplitude profiles show excellent agreement overall. The amplitude profiles for the corresponding difference image track along zero.

We continue to perform RTM for the remaining shots (7 total) and stack across all of the images to perform achieve analysis done on the single shot RTM. Figure 9(b) shows the reference image and Figure 9(a) depicts the image using reconstructed source wavefield for all the shots. The same artifacts due to the source wavefield expanding pass wavelet peak time in Figure 8(c) are present in Figure 9(c). The vertical-like events are crosstalk between receiver wavefield and source wavefield that propagates along x-axis. The amplitude profiles on the RTM image for all shots share the same observations as the single shot images and the difference image amplitude profile is consistently zero.

5 MARMOUSI II EXAMPLE

We further test our method to reconstruct the source wavefield and perform RTM on an anisotropic version of the elastic Marmousi II model (Martin et al., 2006), shown in Figure 10. We calculate the dimensionless Thomsen parameters for vertical transverse isotropy (VTI) ε and δ using the density model with the expressions of $\varepsilon = 0.25\rho - 0.3$ and $\delta = 0.125\rho - 0.125$. We compare the reference source wavefield, Figure 11(a), with the reconstructed wavefield, Figure 11(b). The small amplitude contrasts in the difference plot (Figure 11(c)) are mainly due to the numerical dispersion and the corner points of the boundary used for backward reconstruction. Despite the small differences, we successfully perform RTM using the energy norm imaging condition on the smoothed models for a single shot, seen in Figure 12(a) and all the shots (17 total), seen in Figure 12(b).

6 DISCUSSION

We successfully demonstrate accurate reconstruction of the source wavefield by saving on a single layer on the perimeter of the computational zone in Figure 2(a). Our elastic RTM images demonstrate that our method the representation theorem can produce comparable images to the conventional method utilizing wavefields stored in the entire domain. Our method requires that the single boundary layer adequately samples the source wavefield, i.e., the source wavefield needs to propagate out from the computational zone fully. If parts of the source wavefield do not reach the boundary layer, we are unable to reconstruct that particular portion of the source wavefield. Therefore, our method assumes that the source wavefield exits the computational zone which is reasonable. The introduction of boundaries with well-defined normal vectors such as a superellipse boundary can eradicate the artifacts due to the corners of the computational domain.

7 CONCLUSIONS

We produce accurate elastic RTM image of the subsurface with source wavefield reconstructed synchronously with the receiver wavefield from data stored in a single layer boundary. Reducing the dimension of the stored source wavefield hypercube dramatically reduces the storage requirements for

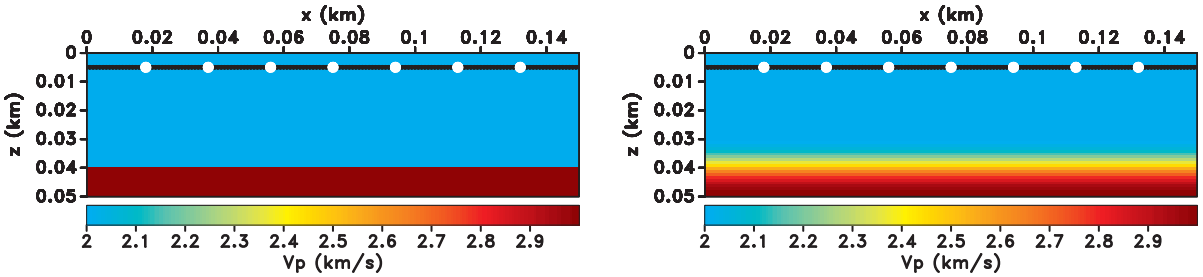


Figure 3. (a) The P-wave velocity model with an overlay of a 2D experiment depicting the source (white dots) and receiver (black line) locations. (b) The corresponding smooth P-wave velocity for reverse time migration.

large 3D imaging problems. Minimal artifacts due to the corners of the computational domain do not impair our ability to image the subsurface accurately and are mostly negligible for most practical applications. The method creates opportunities to accelerate costly techniques implementations such as elastic anisotropic least-squares RTM and full waveform inversion (FWI). The source wavefield reconstruction method presented in this paper applies to media of arbitrary anisotropy and heterogeneity.

8 ACKNOWLEDGMENTS

We would like to thank the sponsors of the Center for Wave Phenomena, whose support made this research possible. The reproducible numeric examples in this paper use the Madagascar open-source software package (Fomel et al., 2013) freely available from http://www.ahay.org.

REFERENCES

Aki, K., and P. G. Richards, 2002, Quantitative seismology.

Anderson, J. E., L. Tan, and D. Wang, 2012, Time-reversal checkpointing methods for RTM and FWI: Geophysics, **77**, S93–S103.

Bo, F., and W. Huazhong, 2011, Reverse time migration with source wavefield reconstruction strategy: Journal of Geophysics and Engineering, **9**, 69.

Clapp, R. G., 2009, Reverse time migration with random boundaries: 79th Annual International Meeting, SEG, Expanded Abstracts, 2809–2813.

Dussaud, E., W. W. Symes, P. Williamson, L. Lemaistre, P. Singer, B. Denel, and A. Cherrett, 2008, Computational strategies for reverse-time migration: 78th Annual International Meeting, SEG, Expanded Abstracts, 2267–2271.

Fomel, S., P. Sava, I. Vlad, Y. Liu, and V. Bashkardin, 2013, Madagascar: open-source software project for multidimensional data analysis and reproducible computational experiments: Journal of Open Research Software, **1**.

Gangi, A. F., 1970, A derivation of the seismic representation theorem using seismic reciprocity: Journal of Geophysical Research, **75**, 2088–2095.

Jia, X., and L. Yang, 2017, A memory-efficient staining algorithm in 3D seismic modelling and imaging: Journal of Applied Geophysics, **143**, 62–73.

Liu, S., X. Li, W. Wang, and T. Zhu, 2015, Source wavefield reconstruction using a linear combination of the boundary wavefield in reverse time migration: Geophysics, **80**, S203–S212.

Martin, G. S., R. Wiley, and K. J. Marfurt, 2006, Marmousi2: An elastic upgrade for marmousi: The Leading Edge, **25**, 156–166.

Mulder, W., 2017, Higher-order source-wavefield reconstruction for reverse-time migration from stored values in a boundary strip just one point wide: Geophysics, **83**, 1–27.

Nguyen, B. D., and G. A. McMechan, 2014, Five ways to avoid storing source wavefield snapshots in 2D elastic prestack reverse time migration: Geophysics, **80**, S1–S18.

Raknes, E. B., and W. Weibull, 2016, Efficient 3D elastic full-waveform inversion using wavefield reconstruction methods: Geophysics, **81**, R45–R55.

Ravasi, M., and A. Curtis, 2013, Elastic imaging with exact wavefield extrapolation for application to ocean-bottom 4C seismic data: Geophysics, **78**, S265–S284.

Rocha, D., N. Tanushev, and P. Sava, 2017, Anisotropic elastic wavefield imaging using the energy norm: Geophysics.

Shen, X., and R. G. Clapp, 2011, Random boundary condition for low-frequency wave propagation: 81st Annual International Meeting, SEG, Expanded Abstracts, 2962–2965.

———, 2015, Random boundary condition for memory-efficient waveform inversion gradient computation: Geophysics, **80**, R351–R359.

Symes, W. W., 2007, Reverse time migration with optimal checkpointing: Geophysics, **72**, SM213–SM221.

Tan, S., and L. Huang, 2014, Reducing the computer memory requirement for 3D reverse-time migration with a boundary-wavefield extrapolation method: Geophysics, **79**, S185–S194.

Vasmel, M., and J. O. Robertsson, 2016, Exact wavefield reconstruction on finite-difference grids with minimal memory requirements: Geophysics, **81**, T303–T309.

Wapenaar, C. P. A., 2014, Elastic wave field extrapolation: Redatuming of single-and multi-component seismic data: Elsevier, **2**.

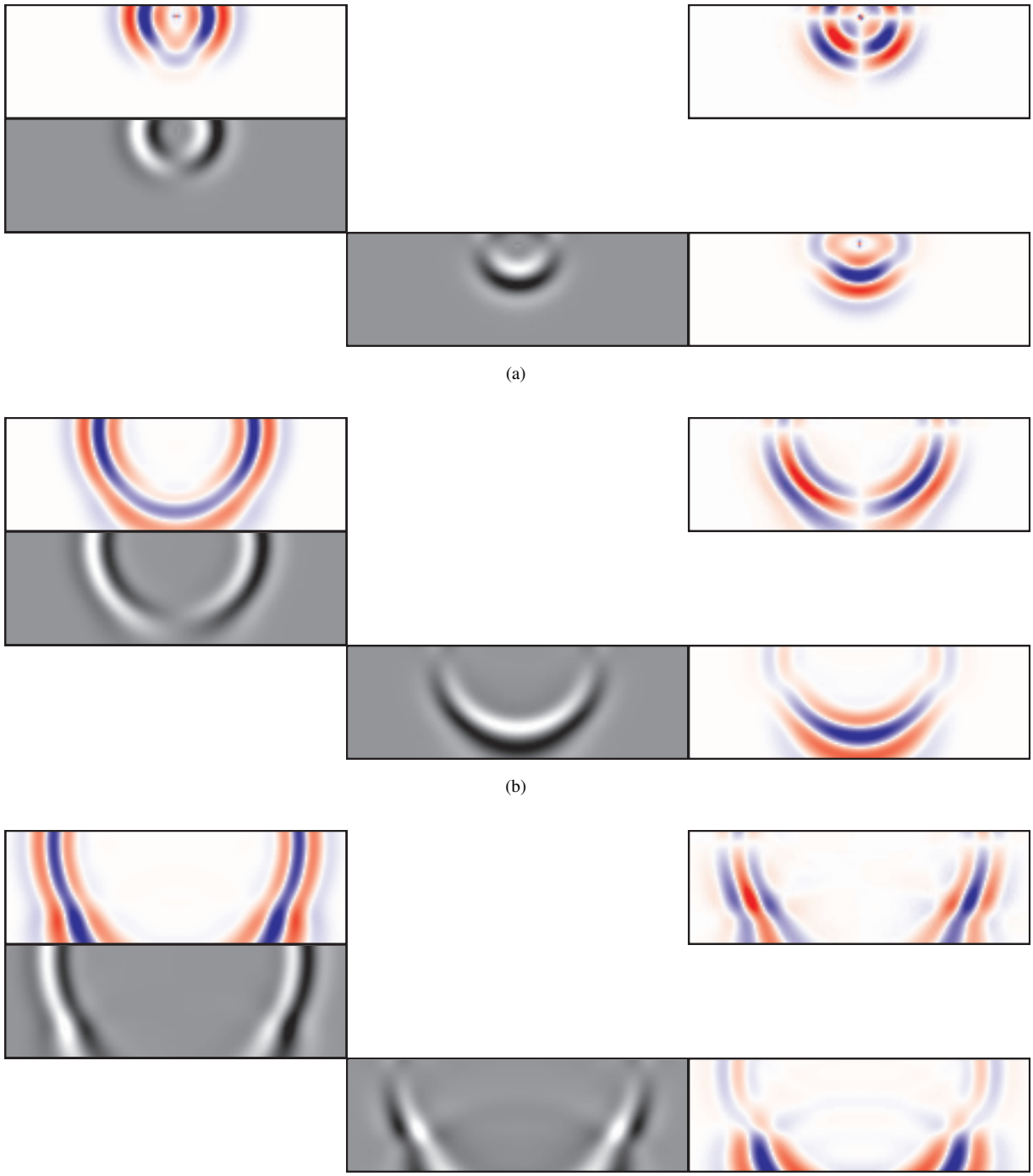
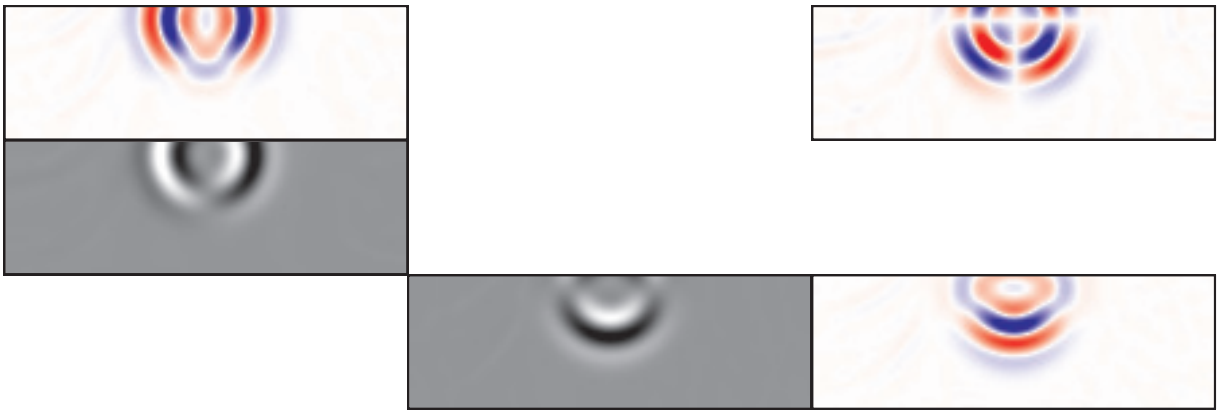


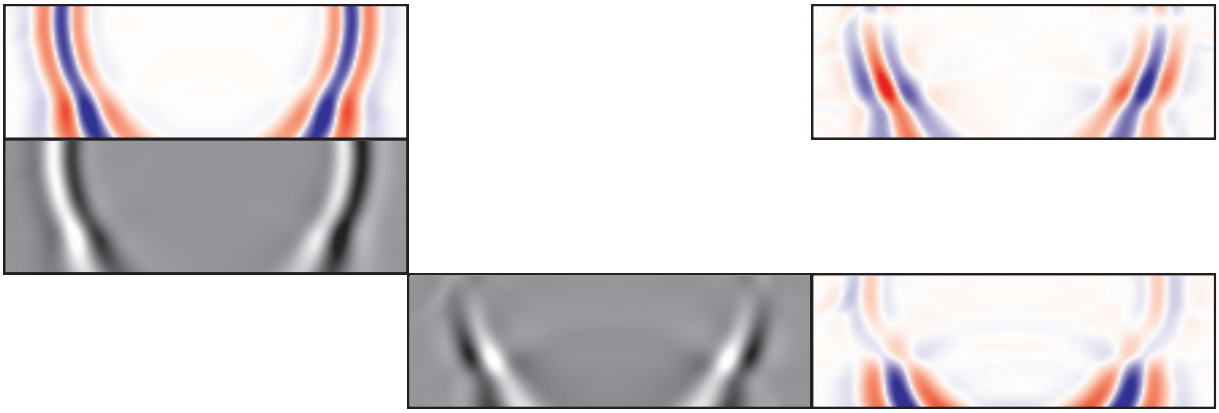
Figure 4. Snapshots of the reference source wavefield for time-step at (a) 200, (b) 300, and (c) 400. The vertical axis of the panels represents the z-axis (depth) whereas the horizontal axis denotes the x-axis (distance). The panels consist of the stress $(\mathrm{t}_{xx}, \mathrm{t}_{zz}, \mathrm{t}_{xz})$ tensor and particle displacement $(\mathrm{u}_x, \mathrm{u}_z)$ vector field in the tensor-vector matrix layout.



(a)

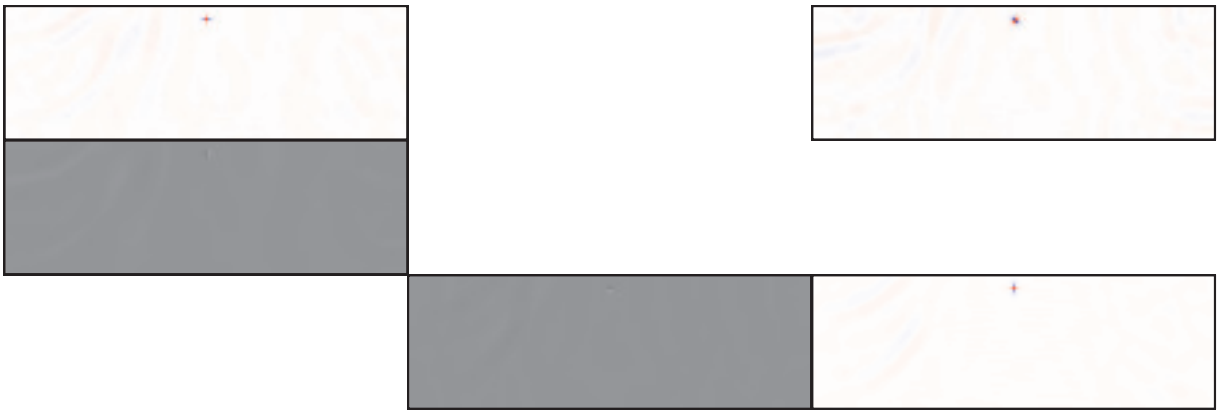


(b)

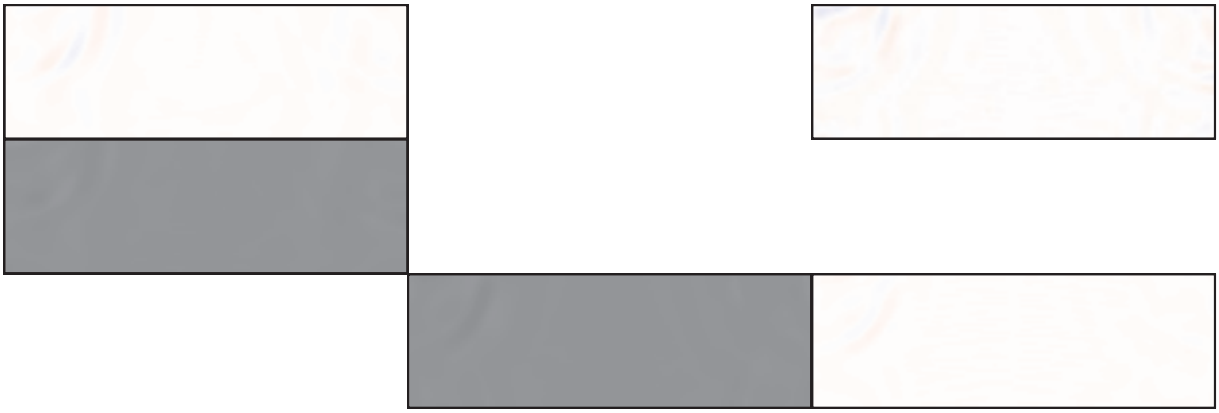


(c)

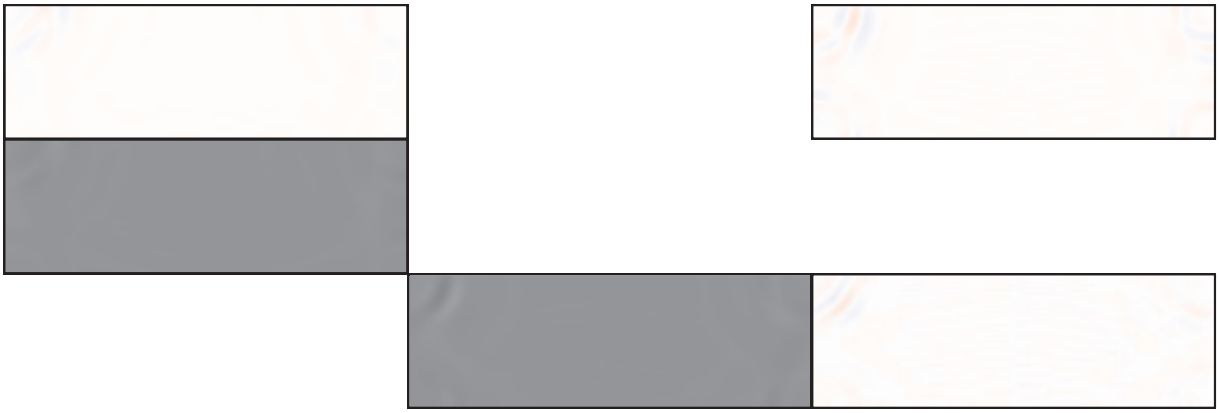
Figure 5. Snapshots of the reconstructed source wavefield from a single boundary layer for time-step at (a) 200, (b) 300, and (c) 400. The vertical axis of the panels represents the z-axis (depth) whereas the horizontal axis denotes the x-axis (distance). The panels consist of the stress $(\mathrm{t}_{xx}, \mathrm{t}_{zz}, \mathrm{t}_{xz})$ tensor and particle displacement $(\mathrm{u}_x, \mathrm{u}_z)$ vector field in the tensor-vector matrix layout.



(a)

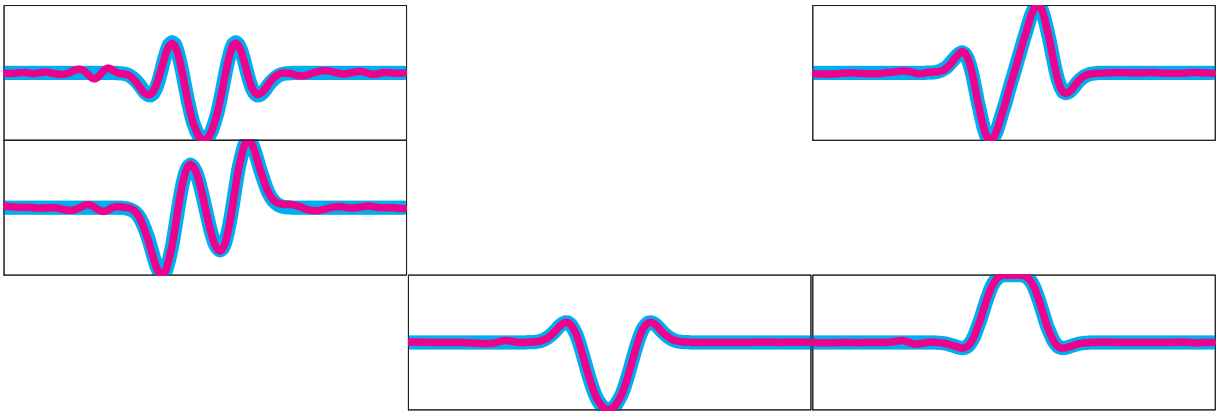


(b)

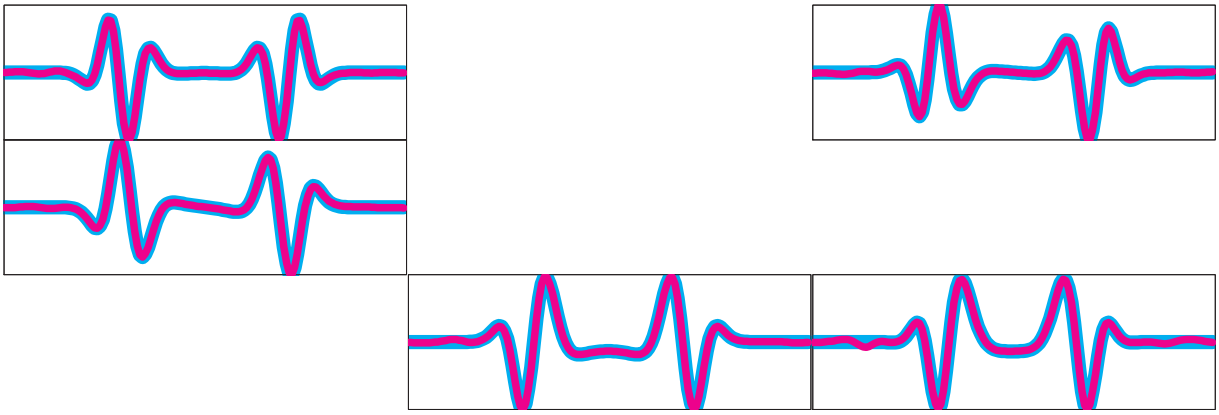


(c)

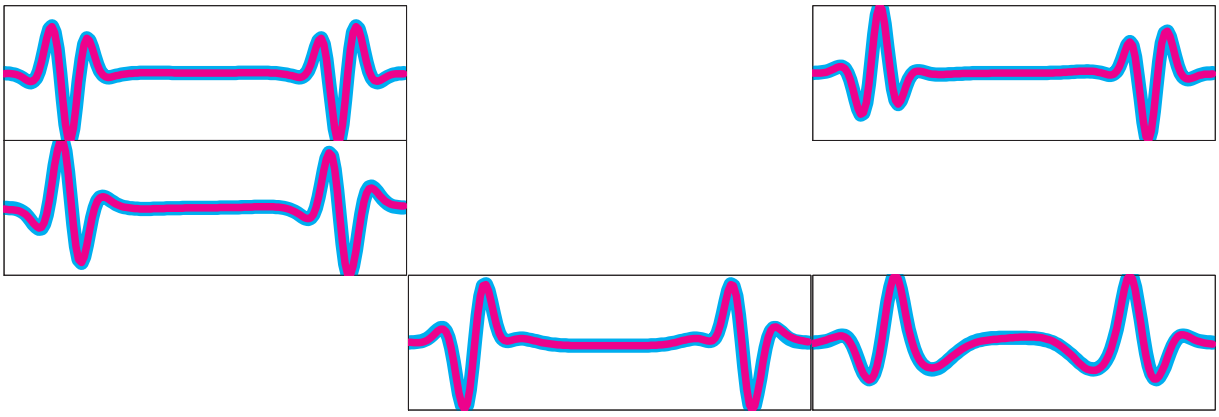
Figure 6. Snapshots of the difference between the forward source wavefield (Figure 4) extrapolation and the reconstructed source wavefield (Figure 5) from the single boundary layer for time-step at (a) 200, (b) 300, and (c) 400. The vertical axis of the panels represents the z-axis (depth) whereas the horizontal axis denotes the x-axis (distance).



(a)



(b)



(c)

Figure 7. Graph along the x-axis at a depth (z-axis) of 0.025 km for the reference source wavefield (in blue) and the reconstructed source wavefield (in red) at time-steps of (a) 200, (b) 300, and (c) 400. The vertical axis of the individual panels represents the amplitude whereas the horizontal axis denotes the x-axis (distance). The panels consist of the stress $(\mathrm{t}_{xx}, \mathrm{t}_{zz}, \mathrm{t}_{xz})$ tensor and particle displacement $(\mathrm{u}_x, \mathrm{u}_z)$ vector field in the tensor-vector matrix layout.

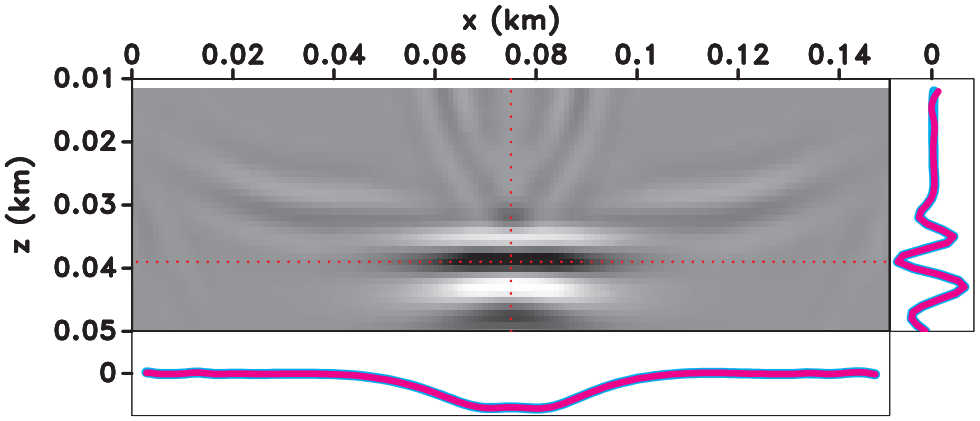


Figure 8. Single shot energy norm elastic reverse time migration using (a) forward source wavefield extrapolation and (b) reconstructed source wavefield. (c) The corresponding difference plot between (a) and (b). The graphs at the bottom of (a), (b), and (c) denotes amplitude profile along the x-axis (horizontal dotted line) at the reflection depth while the graphs on the right show the amplitude profile along the z-axis (vertical dotted line) at the shot location. The blue amplitude profile corresponds to (a), red from (b), and black from (c).

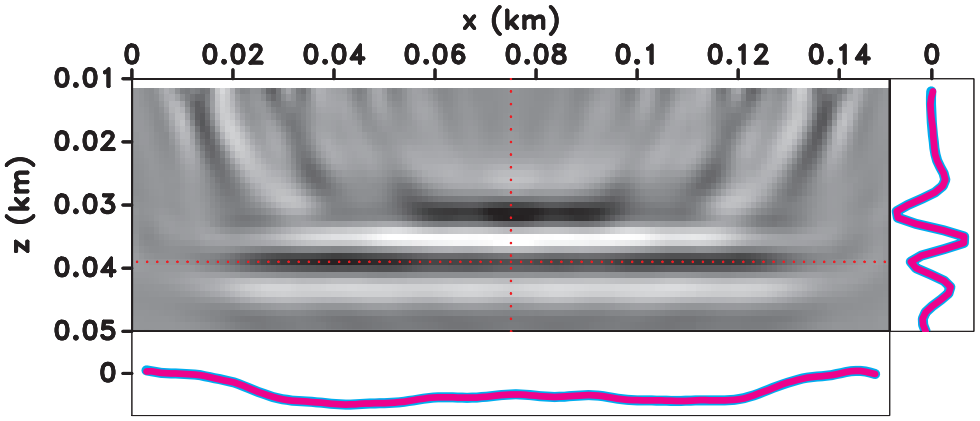


Figure 9. Energy norm elastic reverse time migration from all the available shots using (a) forward source wavefield extrapolation and (b) reconstructed source wavefield. (c) The corresponding difference plot between (a) and (b). The graphs at the bottom of (a), (b), and (c) denotes amplitude profile along the x-axis (horizontal dotted line) at the reflection depth while the graphs on the right show the amplitude profile along the z-axis (vertical dotted line) at the shot location. The blue amplitude profile corresponds to (a), red from (b), and black from (c).

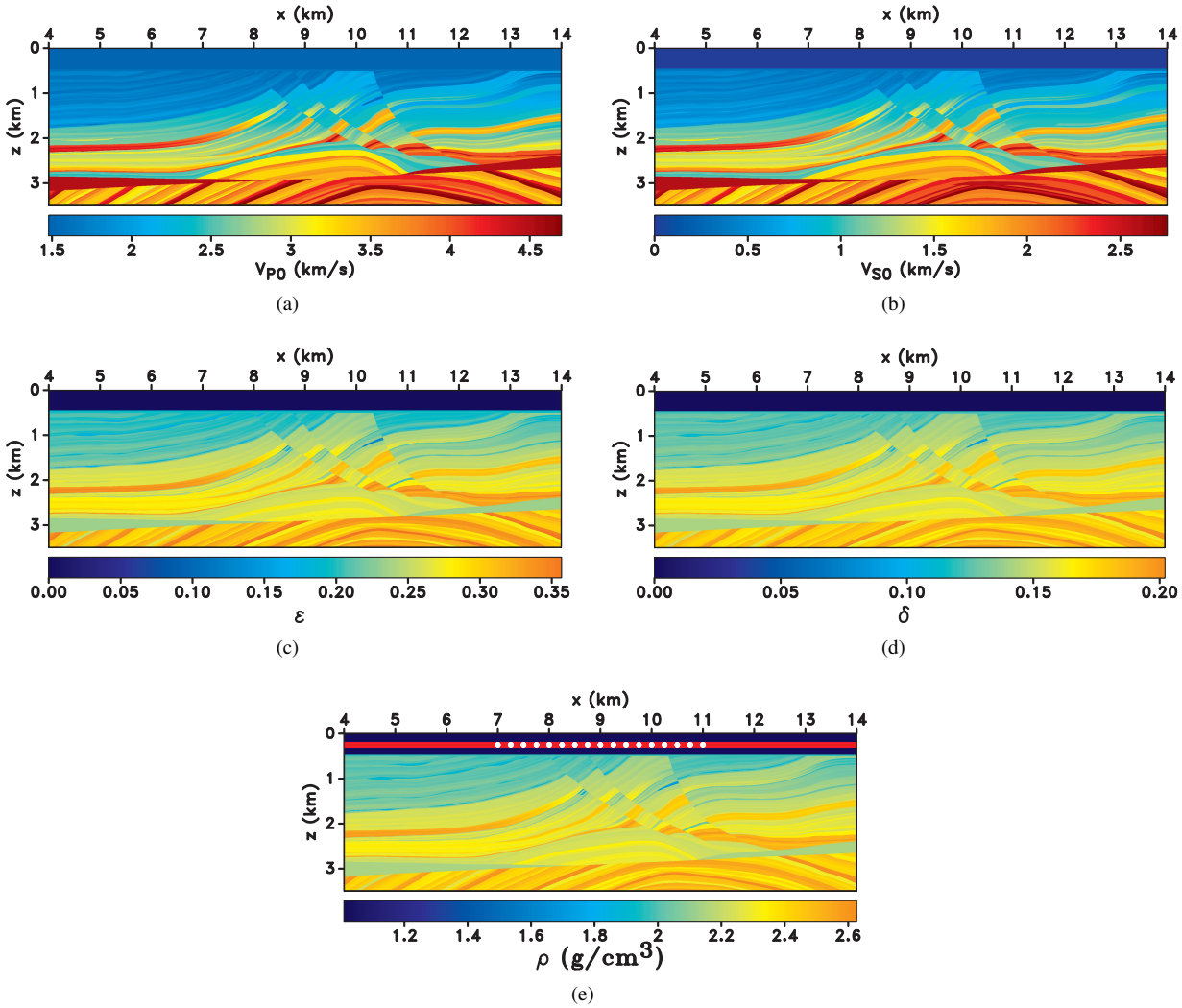
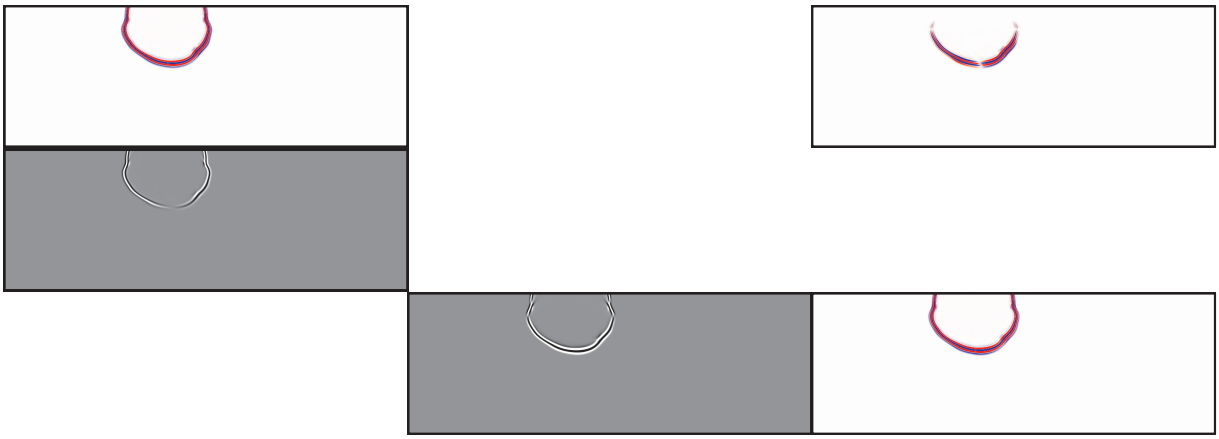


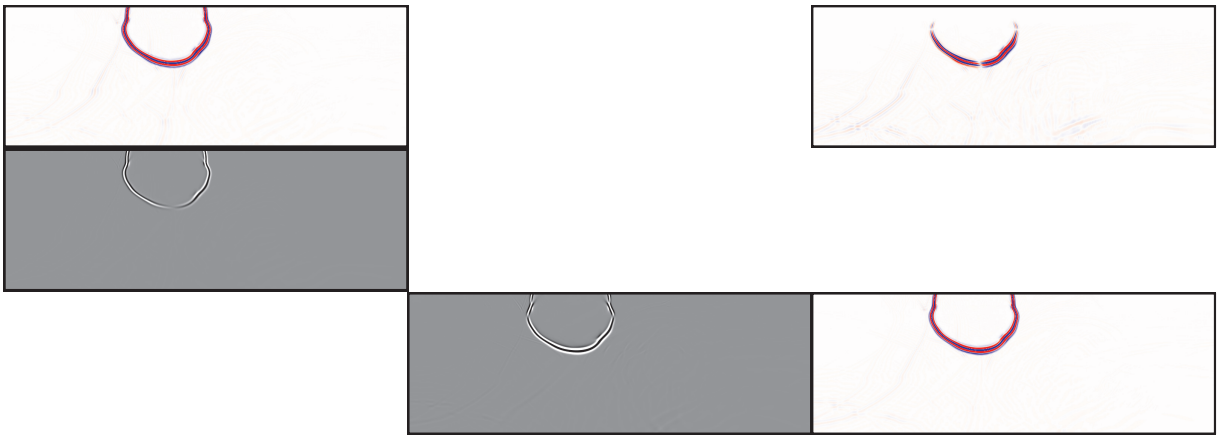
Figure 10. Vertical transverse isotropic Marmousi II model with the vertical (a) P V_{P0} and (b) S V_{S0} velocities. The dimensionless anisotropic Thomsen parameter (c) ε and (d) δ are derived from the (e) density model. The overlay white dots and red line in (e) depict the source and receiver locations respectively.

Yang, P., R. Brossier, and J. Virieux, 2016, Wavefield reconstruction by interpolating significantly decimated boundaries: Geophysics, **81**, T197–T209.

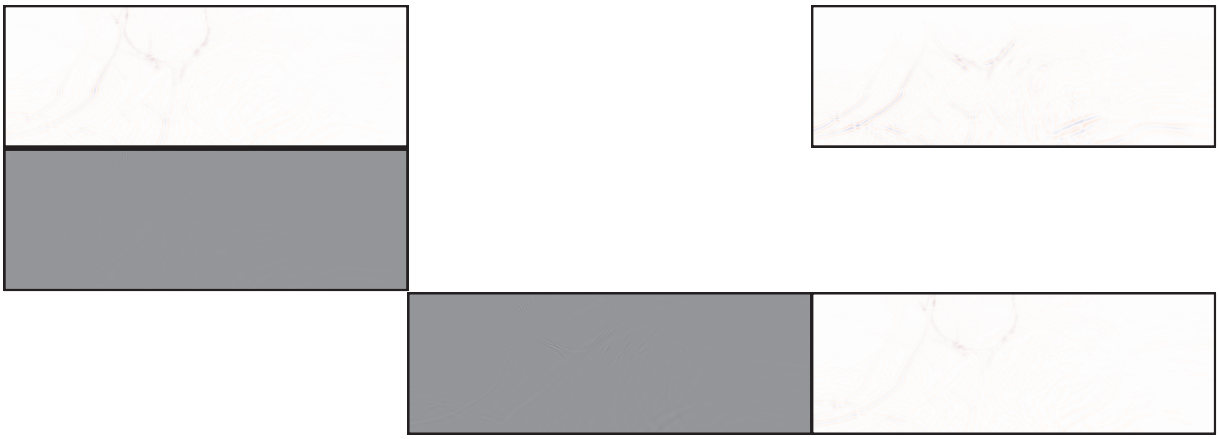
Yang, P., J. Gao, and B. Wang, 2014, RTM using effective boundary saving: A staggered grid GPU implementation: Computers & Geosciences, **68**, 64–72.



(a)

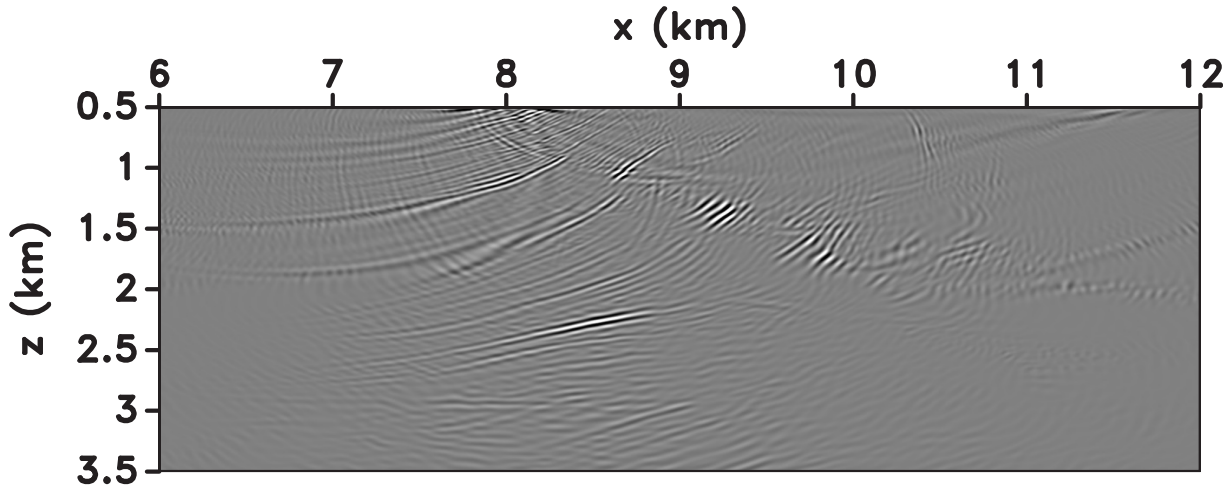


(b)

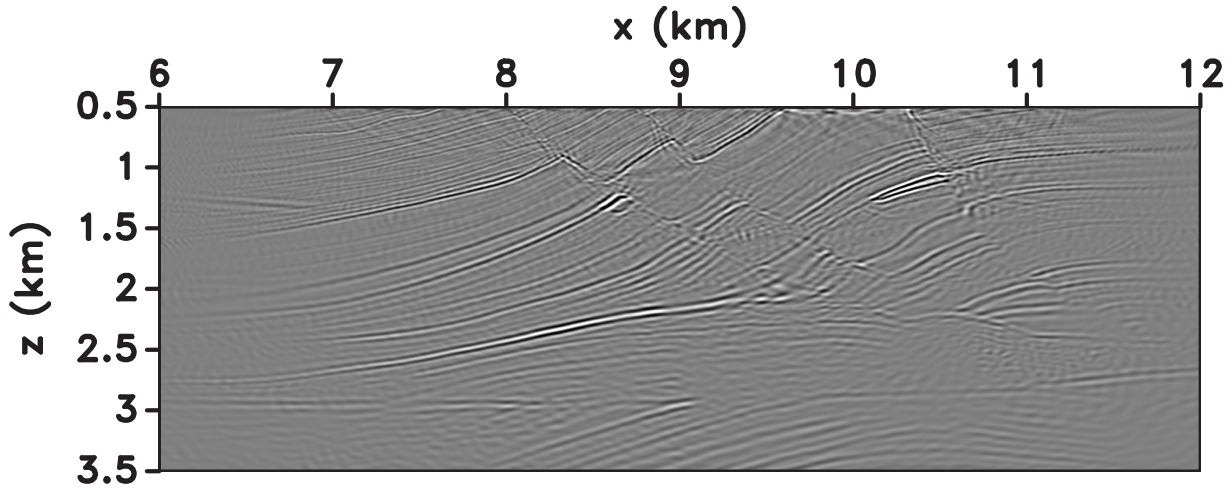


(c)

Figure 11. A snapshot in the anisotropic elastic Marmousi II model in Figure 10 for the (a) reference and (b) reconstructed source wavefields. (c) The corresponding difference between (a) and (b). The vertical and horizontal axes of the panels represent depth and horizontal position. The panels consist of the stress $(\mathrm{t}_{xx}, \mathrm{t}_{zz}, \mathrm{t}_{xz})$ tensor and particle displacement $(\mathrm{u}_x, \mathrm{u}_z)$ vector in the tensor-vector matrix layout.



(a)



(b)

Figure 12. Energy norm elastic reverse time migration for the anisotropic Marmousi II model in Figure 10 using the reconstructed source wavefields for (a) a single shot and (b) all 17 shots.